Comprehensive Laboratory Benchmark of K-shell Dielectronic Satellites of Fe XXV–XXI Ions

Chintan Shah[1,2,3] , Pedro Amaro[4] , Filipe Grilo[4] , Ming Feng Gu[5] , Liyi Gu[6,7] , José Paulo Santos[4] , F. Scott Porter[1] ,
Thomas Pfeifer[2] , Maurice A. Leutenegger[1] , and José R. Crespo López-Urrutia[2]

[1] NASA Goddard Space Flight Center, 8800 Greenbelt Road, Greenbelt, MD 20771, USA; chintan.shah@mpi-hd.mpg.de
[2] Max-Planck-Institut für Kernphysik, Saupfercheckweg 1, 69117 Heidelberg, Germany
[3] Department of Physics and Astronomy, Johns Hopkins University, Baltimore, MD 21218, USA
[4] Laboratory of Instrumentation, Biomedical Engineering and Radiation Physics (LIBPhys-UNL), Department of Physics, NOVA School of Science and
Technology, NOVA University Lisbon, 2829-516 Caparica, Portugal
[5] Space Science Laboratory, University of California, Berkeley, CA 94720, USA
[6] SRON Netherlands Institute for Space Research, Niels Bohrweg 4, 2333 CA Leiden, The Netherlands
[7] Leiden Observatory, Leiden University, P.O. Box 9513, 2300 RA Leiden, The Netherlands
Received 2024 December 15; revised 2025 May 14; accepted 2025 May 19; published 2025 June 25

Abstract

We report on comprehensive laboratory studies of the K-shell dielectronic recombination resonances of Fe XXV–XXI ions that prominently contribute to the hard X-ray spectrum of hot astrophysical plasmas. By scanning a monoenergetic electron beam to resonantly excite trapped Fe ions in an electron beam ion trap and achieving a high electron–ion collision energy resolution of $\sim$7 eV, we resolve their respective KLn satellites up to $n' = 11$. By normalization to known radiative recombination cross sections, we also determine their excitation cross sections and that of the continuum with uncertainties below 15% and verify our results with an independent normalization based on previous measurements. Our experimental data excellently confirm the accuracy and suitability of distorted-wave calculations obtained with the Flexible Atomic Code for modeling astrophysical and fusion plasmas.

Unified Astronomy Thesaurus concepts: Laboratory astrophysics (2004); Atomic physics (2063); Atomic data benchmarking (2064); Experimental techniques (2078); X-ray astronomy (1810); Dielectronic recombination (2061)

Materials only available in the online version of record: machine-readable table

1. Introduction

Most of the baryonic matter in the Universe appears in hot ionized plasmas (10^5–10^7 K) that emit X-rays. They fill intergalactic space (D. Reimers 2002; A. M. Bykov et al. 2008; F. Nicastro et al. 2008, 2018), circumgalactic and interstellar media, and the interiors of stars. Thus, in the last few decades, X-ray astronomy has become indispensable for exploring the high-energy Universe and the extreme physical conditions prevalent in such astrophysical objects (see A. C. Fabian 2023 and references therein). The most prominent and intensively studied features in X-ray spectra are the K-shell emission lines of Fe (M. Asplund et al. 2021) and especially the Kα of helium-like Fe XXV at $\sim$6.7 keV. It is observed by missions such as ASCA, Chandra, XMM-Newton, Suzaku, Hitomi, and XRISM (K. Ebisawa et al. 1996; L. K. Harra-Murnion et al. 1996; A. C. Sterling et al. 1997; J. S. Kaastra et al. 2001; J. R. Peterson et al. 2001; T. Tamura et al. 2001; S. Bianchi et al. 2005; K. Nandra 2006; J. M. Miller et al. 2008; Hitomi Collaboration et al. 2016, 2018; XRISM Collaboration et al. 2024a, 2024b) in active galactic nuclei, supernova remnants, galaxy clusters, and solar flares. The Kα lines from this Fe ion and other lower-charge states serve as critical diagnostics for temperature, ionization state, and elemental abundances in these energetic sources (D. Porquet et al. 2010;

V. Decaux et al. 1995, 1997; J. K. Rudolph et al. 2013; R. Steinbrügge et al. 2022).

The formation of X-ray spectral lines in such environments is governed by a complex interplay of direct processes, such as electron-impact excitation (EIE), and indirect ones, such as dielectronic recombination (DR), resonance excitation, and charge exchange (P. Beiersdorfer et al. 1990; P. Beiersdorfer 2003). In hot plasmas, DR dominates line formation with cross sections several orders of magnitude higher than those of EIE (D. A. Knapp et al. 1989, 1993) and strongly affects the charge-state balance of the plasma (J. Dubau & S. Volonte 1980; P. Beiersdorfer et al. 1992a). First described by H. S. W. Massey & D. R. Bates (1942), its importance was recognized by A. Burgess (1964) for dynamics of hot solar corona plasmas. DR is a two-step resonant mechanism in which a free electron is captured by a positive ion while simultaneously exciting a bound electron. Such doubly excited states decay by emitting distinctive satellite lines in dependence of the electron-energy distribution in resonance with them. Thus, DR satellites serve as sensitive probes of temperature and density, even for non-Maxwellian electron distributions (K. Widmann et al. 1995; P. Beiersdorfer et al. 1992a, 1993; T. Kato et al. 1998; R. Radtke et al. 2000; L. Gu et al. 2020).

Recent astrophysical observations have highlighted both the potential and the challenges of DR-based diagnostics. The high-resolution spectrum of the Perseus cluster obtained by the Hitomi X-ray Observatory in 2016 (Hitomi Collaboration et al. 2016) revealed serious discrepancies between often-used

atomic databases and spectral fitting codes such as atomDB/APEC (A. R. Foster et al. 2012), SPEX (J. S. Kaastra et al. 1996), and CHIANTI (G. Del Zanna et al. 2015). The observed Kα complex of Fe XXV consists of four main transition lines (w, x, y, and z) excited by EIE with mostly unresolved contributions from DR satellites. Inconsistencies in their positions and cross sections across the aforementioned models led to 15%–20% variations in the derived plasma parameters (Hitomi Collaboration et al. 2018). Furthermore, high-$n \geqslant 3$ DR satellites blend on the red side of the resonance line w and can easily cause apparent line broadening and shifts of Kα. Without proper accounting, this introduces inaccuracies in the analysis of temperature, velocity, and turbulence in astrophysical and laboratory fusion plasmas (P. Beiersdorfer et al. 1992b). Improving our understanding of DR processes is thus essential to fully exploit the capabilities of X-ray observatories equipped with high-resolution calorimeter-based missions, such as XRISM (M. Tashiro et al. 2018), which was launched last year and has already started taking observations (XRISM Collaboration et al. 2024a, 2024b), and the upcoming Athena (F. Pajot et al. 2018).

In the last decades, many experimental and theoretical studies of DR of highly charged ions (HCIs) were reported. Intrashell ($\Delta n = 0$) low-energy DR rate coefficients, important for low-temperature photoionized plasmas, were measured at storage rings (D. W. Savin et al. 2002aa, 2002b; M. Schnell et al. 2003; D. V. Lukić et al. 2007; I. Orban et al. 2010), while intershell ($\Delta n = 1$) DR strengths and rate coefficients, which are crucial for high-temperature collisionally ionized plasmas, were studied in electron-beam ion traps (EBITs; D. A. Knapp et al. 1989, 1993; T. Fuchs et al. 1998; A. J. Smith et al. 2000; B. E. O'Rourke et al. 2004; X. Zhang et al. 2004; A. J. González Martínez et al. 2005; N. Nakamura et al. 2008; C. Beilmann et al. 2009; K. Yao et al. 2010; S. Ali et al. 2011; C. Beilmann et al. 2011; Z. Hu et al. 2013; C. Shah et al. 2015, 2016; P. Amaro et al. 2017; C. Shah et al. 2018; Z. Harman et al. 2019). DR measurements on highly charged Fe ions mostly focused on the resonance strengths of entire regions (KLL, KLM) of helium-like Fe XXV and could resolve neither level nor satellites beyond $n' \geqslant 6$ and were not charge-state specific (P. Beiersdorfer et al. 1992a, 1992b, 1993; H. Watanabe et al. 2001). Here, KLL denotes an analogy to the time-reversed process of Auger–Meitner decay, the dielectronic capture process where a free electron recombines into the L-shell by resonantly exciting a bound electron from the K to the L shell.

We fill these critical gaps in essential experimental data by targeted comprehensive measurements of K-shell DR resonances of Fe XXV–XXI ions with an EBIT. Our outstanding electron-beam energy resolution of about 7 eV allows us to resolve KLn satellites up to $n' = 11$. With these data, we determined DR resonance strengths with uncertainties below ~15%. Our results agree overall very well with atomic structure and distorted wave calculations performed with the Flexible Atomic Code (FAC; M. F. Gu 2008) including EIE. Our accurate benchmarking of this code recommends its use in generating the atomic data sets needed for astrophysical and fusion plasma models.

2. Measurements

We employ FLASH-EBIT (S. W. Epp et al. 2007, 2010) for the present experiment. In this device, a nearly monoenergetic electron beam is produced by a barium oxide dispenser cathode, with currents ranging from tens to hundreds of milliamperes. The beam is compressed by a 6 T superconducting magnet in Helmholtz configuration to a diameter of less than 50 μm (C. Shah et al. 2018). Iron was continuously injected into the trap region in the form of iron pentacarbonyl (Fe(CO)$_5$) molecules through a two-stage differential pumping system. After dissociation of this molecule by the electron beam, the Fe atoms experience successive electron-impact ionization, yielding HCI, which are radially trapped in the negative space charge potential of the electron beam and axially confined by electrostatic potentials applied to the cylindrical drift-tube electrodes surrounding the trap region.

We swept the electron-beam energy over a range of KLn resonances, whereby a free electron is captured in one of the n shells upon exciting a bound electron from the K to the L shell. For this we vary the drift-tube platform voltage, which biases all the drift tubes, from 2.1 to 5.1 kV in a triangular wave pattern at a slew rate of 50 V s^{-1}. This, in addition to the 2 kV negative bias applied to the cathode, yields electrons of the required kinetic energies. In order to enhance the electron-beam energy resolution, we reduce the nominal axial trapping potential to only 10 V while keeping the current at 100 mA to ensure enough production of Fe HCIs. We optimize the axial trap depth and beam current, together with the Fe(CO)$_5$ injection pressure, to force evaporative cooling of the trapped ions, resulting in a small characteristic ion gyroradius that samples only a fraction of the space-charge distribution of the electron beam (B. M. Penetrante et al. 1991b; C. Beilmann et al. 2009; C. Shah et al. 2016). This gives us a relative electron-energy resolution of $E/\Delta E \approx 900$ at 6.5 keV, nearly 10 times better than earlier Fe works (P. Beiersdorfer et al. 1992a, 1992b; H. Watanabe et al. 2001). This allows us to observe the DR satellites maximum up to $n' = 11$ contributing to Fe K-shell X-ray lines (see Figure 1). We dump the ion content of the trap for 3 s at the end of each 60 s sweep cycle to prevent a slow accumulation of Ba and W ions generated from atoms emanating from the hot cathode.

X-rays from the radiative decay of doubly excited KLn DR resonances were recorded over 20 hr using a silicon drift detector (SDD) with an energy resolution of ~120 eV FWHM at ~6 keV while sweeping the electron beam energy. The resulting two-dimensional (2D) intensity histogram of X-ray energy versus electron-beam energy is shown in Figure 1. The diagonal bands visible there correspond to radiative recombination (RR) into states with principal quantum numbers $n = 2$ and $n = 3$. Here, the X-ray energy is the sum of free electron energy and binding energy of the L and M shell, respectively. Bright spots between the solid lines encompassing X-rays of about 6.7 keV are due to the $n = 2 \rightarrow 1$ radiative decay following the formation of doubly excited KLn DR states, where $n = 2, 3, 4$, etc. The clustered resonances between 4500 and 5000 eV beam energy arises from KLL DR resonances of Fe XXV–XXI ions. Resonances from lower-charge states of Fe appear at lower photon energies since more bound electrons screen the nuclear potential for the $n = 2$ electrons. At 5800 eV electron-beam energy, the KLM resonances appear, which can radiatively decay either by $n = 2 \rightarrow 1$ or $n = 3 \rightarrow 1$, thus emitting Kα or Kβ photons, respectively. Analogous radiative decay pathways of higher KLn, where n is up to 11, and DR resonances appear at higher beam energies and merge above a threshold around 6.5 keV with the direct EIE of the $1s - np$ transitions.
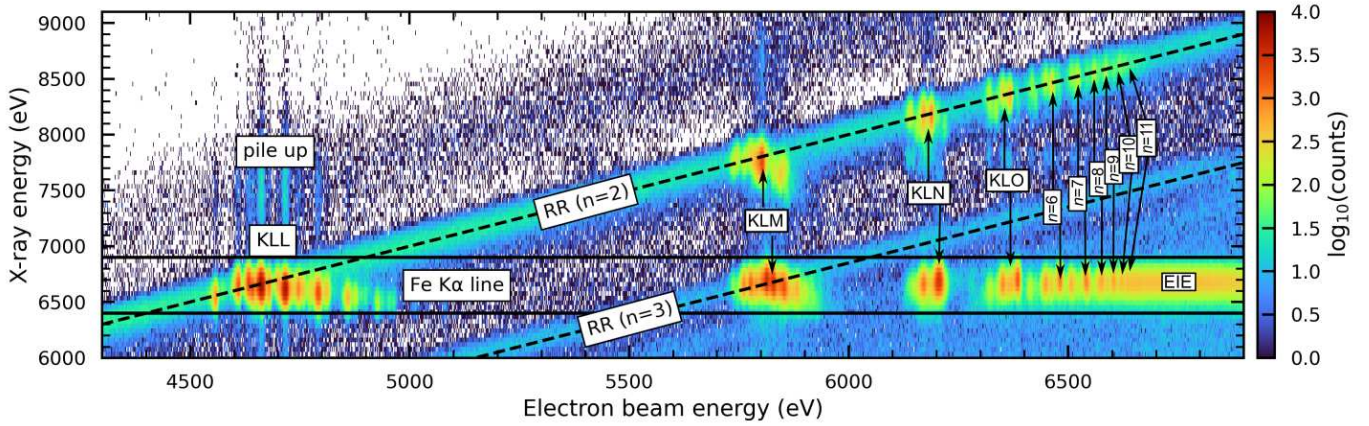
Figure 1. Intensity histogram of energy-resolved X-ray emission of Fe ions vs. electron-beam energy. The solid lines contain the DR satellite channels of Kα at $\sim$6.7 keV resolved up to $n = 11$. Two diagonal dashed lines mark radiative recombination (RR) into $n = 2$ and 3 shells. Above the RR $n = 2$ line, artifacts due to their pileup with L-shell emissions below 2 keV are visible.

3. Theoretical Calculations

Theoretical studies have extensively examined the KLL DR resonances of Fe XXV, e.g., F. Bely-Dubau et al. (1979), M. H. Chen (1986), J. Nilsen (1988), P. Beiersdorfer et al. (1992a), S. N. Nahar et al. (2001), M. F. Gu (2003), S. Sardar et al. (2018), and C. Shah et al. (2018). However, calculations for KL$n > 2$ DR and other lower-charge states of Fe contributing to the K shell X-ray lines remain scarce. In this work, we used FAC to compute all possible KLn DR channels using a fully relativistic configuration interaction (CI) method, treating continuum states within the relativistic distorted wave approximation (see M. F. Gu 2008 and references therein). The independent-resonance approximation model is used to evaluate the DR resonance energies and strengths.

For this, we included sets of initial configurations as $[1s^2 (nl)^e, 1s^1 (nl)^{e+1}, 1s^1 (nl)^e n'l', \text{and } 1s^2 (nl)^{e-1} n'l']$, sets of intermediate doubly excited configurations as $[1s^1 (nl)^{e+2}$ and $1s^1 (nl)^e n'l']$, and sets of final configurations as $[1s^2 (nl)^{e+1}$ and $1s^2 (nl)^e n'l']$ in our structure calculations. The number of electrons, e, ranges from zero to four, covering Fe XXV through Fe XXI ions. Furthermore, n has been limited to 2, since the maximum electron-beam energy in the present experiment is below 7 keV. n' values are included up to 15 and $l\,l'$ up to 8. Higher ($l > 8$) contributions are expected to be negligible (M. F. Gu 2003).

Table 1 presents a comparison of our present FAC energy calculations with previously reported results. The available literature focuses primarily on KLL DR resonance energies of Fe XXV and their satellite transition energies in Fe XXIV, limiting the scope of our comparison. The most advanced CI energy level calculations for Fe XXIV are available in the literature (V. A. Yerokhin & A. Surzhykov 2012, 2018; V. I. Azarov et al. 2023), with accuracies surpassing the available experimental results (P. Beiersdorfer et al. 1993; J. K. Rudolph et al. 2013; R. Steinbrügge et al. 2022). FAC, in comparison to these advanced calculations, deviate up to $\sim \pm 2$ eV on an absolute scale. However, the relative differences are on the order of 0.5–1 eV, likely due to differences in the calculations of ground-state energy. Nonetheless, our FAC predictions agree within $\sim 0.02\%$ with these state-of-the-art calculations.

Experimental values measured using the crystal spectrometer at Princeton Large Torus tokamak (P. Beiersdorfer et al. 1993)

show deviations of up to 2σ–2.5σ with respect to our FAC results. We note that some of the experimental line accuracies reported in this work are affected by line blends. The high-resolution synchrotron experiment (J. K. Rudolph et al. 2013) measured four Fe XXIV transitions, which, with an exception of u, agree with our FAC predictions within 1 eV. The present FAC, in comparison with older calculations by L. A. Vainshtein & U. I. Safronova (1978), show differences of up to 2–4 eV, while more recent multiconfiguration Dirac–Fock calculations (S. Sardar et al. 2018) differ by up to 2 eV. The resonance energies reported in P. Beiersdorfer et al. (1992a) are consistently lower than our FAC predictions, with deviations ranging from 0.6 to 4 eV. Our previous work (C. Shah et al. 2018) also reported KLL DR resonance energies for Fe XXV through Fe XIX ions and found an average deviation of 1.3 eV from our previous FAC calculations.

Beyond KLL transitions, no additional data are available in the literature. Thus, we provide complete energy level calculations for Fe XXV through Fe XXI, up to $n' = 15$, as machine-readable files. An excerpt is shown in Table 2.

To determine DR resonance strengths, we also used FAC to calculate dielectronic capture strengths, radiative and auto-ionization transition rates, and branching ratios. All these values for ions under this study are provided in the machine-readable files. Table 2 lists partial KLn DR resonance data for the Fe XXV ion, including their intermediate doubly excited and final state configurations, as well as their resonance energies, photon energy, branching ratio, and strengths. These data could potentially support comparisons and updates to atomic data incorporated into spectral models such as AtomDB (A. R. Foster et al. 2012), SPEX (J. S. Kaastra et al. 1996), and CHIANTI (G. Del Zanna et al. 2015).

Our theoretical data also facilitate the calculation the K-shell DR rate coefficient, which is an essential quantity for modeling collisionally ionized plasmas found in astrophysical and laboratory fusion plasma environments. Using the rate coefficient formula from M. F. Gu (2003), we compute DR rates and compare them with data from the widely used OPEN-ADAS database.[8] The OPEN-ADAS rates, mainly derived from AUTOSTRUCTURE (N. R. Badnell 1986), are available in both Russell–Saunders LS coupling and

---

[8] https://open.adas.ac.uk/

Table 1
Present FAC Predictions of KLL DR Resonance and X-Ray Satellite Transition Energies of Fe XXV Compared with Available Calculations and Experimental Results

Line	Transition	Resonance Energy		X-Ray Satellite Energy					
		This Work[a]	B92[b]	This Work[a]	Y12[c]	Y18[d]	S18[e]	VS[f]	Previous Experiments
a	$1s2p^2(^3P)\,^2P_{3/2} \to 1s2p_{3/2}\,^2P^o_{3/2}$	4679.1	4677.0 (2.10)	6658.09	6658.12(1) (−0.03)	6658.12(3) (−0.03)	6659.37 (−1.28)	6659.73 (−1.64)	6658.41(107)[g] (−0.32)
b	$1s2p^2(^3P)\,^2P_{3/2} \to 1s2p_{1/2}\,^2P^o_{1/2}$	4679.1	4677.0 (2.10)	6673.94	6674.08(1) (−0.15)	6674.08(3) (−0.15)	6675.15 (−1.21)	6675.51 (−1.57)	⋯
c	$1s2p^2(^3P)\,^2P_{1/2} \to 1s2p_{3/2}\,^2P^o_{3/2}$	4660.8	4658.6 (2.20)	6639.86	6639.86(1) (0.01)	6639.86(3) (0.00)	6640.82 (−0.96)	6641.89 (−2.03)	⋯
d	$1s2p^2(^3P)\,^2P_{1/2} \to 1s2p_{1/2}\,^2P^o_{1/2}$	4660.8	4658.6 (2.20)	6655.71	6655.82(1) (−0.11)	6655.83(3) (−0.12)	6656.87 (−1.16)	6657.58 (−1.88)	⋯
e	$1s2p^2(^3P)\,^4P_{5/2} \to 1s2p_{3/2}\,^2P^o_{3/2}$	4639.6	4639.0 (0.60)	6618.66	6620.35(1) (−1.69)	6620.31(3) (−1.65)	6621.67 (−3.01)	6622.73 (−4.07)	6621.46(124)[g] (−2.80)
f	$1s2p^2(^3P)\,^4P_{3/2} \to 1s2p_{3/2}\,^2P^o_{3/2}$	4633.5	4632.9 (0.60)	6612.52	6614.4(1) (−1.88)	6614.36(3) (−1.84)	6615.31 (−2.79)	6616.73 (−4.20)	⋯
g	$1s2p^2(^3P)\,^4P_{3/2} \to 1s2p_{1/2}\,^2P^o_{1/2}$	4633.5	4632.9 (0.60)	6628.37	6630.37(1) (−2.00)	6630.33(3) (−1.96)	6631.23 (−2.87)	6632.30 (−3.93)	⋯
h	$1s2p^2(^3P)\,^4P_{1/2} \to 1s2p_{3/2}\,^2P^o_{3/2}$	4625.3	4624.6 (0.70)	6604.28	6606.05(1) (−1.76)	6606.01(3) (−1.73)	6607.20 (−2.92)	6608.61 (−4.33)	⋯
i	$1s2p^2(^3P)\,^4P_{1/2} \to 1s2p_{1/2}\,^2P^o_{1/2}$	4625.3	4624.6 (0.70)	6620.13	6622.01(1) (−1.88)	6621.98(3) (−1.85)	6623.09 (−2.96)	6624.15 (−4.02)	⋯
j	$1s2p^2(^1D)\,^2D_{5/2} \to 1s2p_{3/2}\,^2P^o_{3/2}$	4665.3	4664.1 (1.20)	6644.34	6644.67(1) (−0.33)	6644.64(3) (−0.30)	6646.16 (−1.83)	6646.52 (−2.18)	6645.24(43)[g] (−0.90)
k	$1s2p^2(^1D)\,^2D_{3/2} \to 1s2p_{1/2}\,^2P^o_{1/2}$	4659.8	4658.1 (1.70)	6654.62	6654.79(1) (−0.16)	6654.76(3) (−0.13)	6656.15 (−1.53)	6656.87 (−2.25)	6654.19(71)[g] (0.43)
l	$1s2p^2(^1D)\,^2D_{3/2} \to 1s2p_{3/2}\,^2P^o_{3/2}$	4659.8	4658.1 (1.70)	6638.78	6638.82(1) (−0.04)	6638.79(3) (−0.01)	6640.47 (−1.69)	6641.18 (−2.40)	⋯
m	$1s2p^2(^1S)\,^2S_{1/2} \to 1s2p_{3/2}\,^2P^o_{3/2}$	4699.4	4697.7 (1.70)	6678.38	6677.65(2) (0.73)	6677.62(3) (0.76)	6679.82 (−1.44)	6679.46 (−1.08)	6676.84(72)[g] (1.54)
n	$1s2p^2(^1S)\,^2S_{1/2} \to 1s2p_{1/2}\,^2P^o_{1/2}$	4699.4	4697.7 (1.70)	6694.23	6693.62(2) (0.61)	6693.58(3) (0.64)	6695.70 (−1.47)	6694.97 (−0.75)	⋯
o	$1s2s^2\,^2S_{1/2} \to 1s2p_{3/2}\,^2P^o_{3/2}$	4555.6	4553.4 (2.20)	6534.67	6536.37(3) (−1.71)	6536.3(3) (−1.64)	6537.18 (−2.52)	6538.22 (−3.55)	6536.49(69)[g] (−1.83)
p	$1s2s^2\,^2S_{1/2} \to 1s2p_{1/2}\,^2P^o_{1/2}$	4555.6	4553.4 (2.20)	6550.51	6552.34(3) (−1.83)	6552.27(3) (−1.76)	6553.08 (−2.57)	6553.77 (−3.26)	6552.42(87)[g] (−1.91)
q	$1s2s2p(^3P^o)\,^2P^o_{3/2} \to 1s2s\,^2S_{1/2}$	4618.1	4615.3 (2.80)	6662.45	6662.19(1) (0.26)	6662.19(3) (0.26)	6663.31 (−0.86)	6664.03 (−1.58)	6662.09(54)[g], 6662.24(7)[h] (0.36)[g], (0.21)[h]
r	$1s2s2p(^3P^o)\,^2P^o_{1/2} \to 1s2s\,^2S_{1/2}$	4608.9	4604.9 (4.00)	6653.26	6652.78(2) (0.49)	6652.79(3) (0.47)	6653.65 (−0.39)	6655.08 (−1.82)	6654.19(71)[g], 6652.83(7)[h] (−0.93)[g], (0.43)[h]
s	$1s2s2p(^1P^o)\,^2P^o_{3/2} \to 1s2s\,^2S_{1/2}$	4635.8	4633.2 (2.60)	6680.10	6679.11(6) (0.99)	6679.1(3) (1.00)	6680.90 (−0.81)	6681.26 (−1.17)	⋯
t	$1s2s2p(^1P^o)\,^2P^o_{1/2} \to 1s2s\,^2S_{1/2}$	4632.6	4631.2 (1.40)	6676.94	6676.13(5) (0.81)	6676.11(3) (0.84)	6678.02 (−1.08)	6678.38 (−1.44)	6676.84(72)[g], 6676.20(7)[h] (0.11)[g], (−0.74)[h]

Table 1
(Continued)

Line	Transition	Resonance Energy		X-Ray Satellite Energy					
		This Work[a]	B92[b]	This Work[a]	Y12[c]	Y18[d]	S18[e]	VS[f]	Previous Experiments
u	$1s2s2p(^3P^o)\,^4P^o_{3/2} \rightarrow 1s^22s\,^2S_{1/2}$	4570.9	4570.1	6615.20	6616.56(1)	6616.55(3)	6617.78	6618.84	6617.89(124)[g], 6616.63 (7)[h,i]
			(0.80)		(−1.36)	(−1.35)	(−2.58)	(−3.64)	(−2.69)[g], (−1.43)[h,i]
v	$1s2s2p(^3P^o)\,^4P^o_{1/2} \rightarrow 1s^22s\,^2S_{1/2}$	4567.1	4566.3	6611.45	6612.85(1)	6612.84(3)	6613.90	6614.96	6612.94(7)[i]
			(0.80)		(−1.40)	(−1.39)	(−2.45)	(−3.51)	(−1.49)[i]

Notes. All energy values are expressed in eV, with line labels following the notation of A. H. Gabriel & C. Jordan (1969). The CODATA2018 (E. Tiesinga et al. 2021) recommended value of hc was used to convert literature values from Å to eV. Values in round parentheses below the theoretical values denote the absolute differences from the present FAC calculations.
[a] This work: present FAC calculation.
[b] B92: P. Beiersdorfer et al. (1992a).
[c] YS12: V. A. Yerokhin & A. Surzhykov (2012).
[d] YS18: V. A. Yerokhin & A. Surzhykov (2018).
[e] S18: S. Sardar et al. (2018).
[f] VS: L. A. Vainshtein & U. I. Safronova (1978), P. Beiersdorfer et al. (1992a).
[g] P. Beiersdorfer et al. (1993).
[h] J. K. Rudolph et al. (2013).
[i] R. Steinbrügge et al. (2022).

intermediate intermediate coupling (IC) coupling formats for Fe XXV (M. A. Bautista & N. R. Badnell 2007), Fe XXIV (J. Colgan et al. 2004), and Fe XXIII (J. Colgan et al. 2003). We note that these rates are also used in the APEC/AtomDB (A. R. Foster et al. 2012) spectral model used in the X-ray astrophysics community. Figure 2 compares our derived DR rate coefficients with those in the OPEN-ADAS database for electron temperatures ranging from 0.5 to 200 keV. Our calculated rates for Fe XXIV and Fe XXIII are slightly lower compared to those from OPEN-ADAS, whereas we find good agreement for Fe XXV. Overall, FAC and OPEN-ADAS DR rates agree within 10%.

For comparison with our present EBIT experiment, as shown in our previous work (C. Shah et al. 2019), we fed atomic data into the collisional-radiative model of FAC, which solves population balance equations on a fine grid of the beam energy, matching the present experimental conditions (M. F. Gu 2008). The resulting level populations enter the calculations of total line emission cross sections from both DR and EIE processes as a function of electron-beam energy. Additionally, since we observed X-rays following RR into the L and M shells of Fe ions, we calculate total RR cross sections with FAC, finding agreement within $\sim$4% with those previously reported by H. Chen et al. (2005).

The unidirectional electron beam in an EBIT leads to polarized and anisotropic X-ray emission following RR and DR processes (J. R. Oppenheimer 1927; J. R. Henderson et al. 1990; P. Beiersdorfer et al. 1996; H. Chen et al. 2005; C. Shah et al. 2015). Since our SDD detector is mounted at 90° with respect to the electron-beam propagation axis, observed RR and DR X-ray intensities require corrections for polarization effects. Using FAC, we calculate polarization correction factors, accounting for depolarization effects arising from the cyclotron motion of electrons within the electron beam and radiative cascades (M. F. Gu et al. 1999). For the former, we apply a transverse energy component of $\sim$450 eV, measured in

our previous study (C. Shah et al. 2018), to our FAC polarization calculations.

4. Data Analysis and Discussion of the Results

4.1. K-shell Cross Sections: KLn DR Satellites

In addition to determining the DR line energies, we also infer the cross sections for all the observed satellite lines and compare them with predictions. To do this, we need to convert the observed X-ray counts into absolute cross sections. However, due to the unknown electron-beam density, ion-number density, and overlap factor between electron beam and ion cloud, absolute cross sections cannot be directly determined. Nonetheless, as shown by D. A. Knapp et al. (1989) and P. Beiersdorfer et al. (1992a), we can use the theoretical cross sections of RR into $n = 2$, observed in this experiment, to normalize the DR satellites.

For this procedure, the charge-state distribution must be known. However, strong DR resonances modify it. In principle, this distribution can be estimated by comparing the experimental data with theoretical DR resonance strengths for each charge state, assuming a steady-state charge balance is achieved during a sufficiently slow electron-beam-energy scan. It is known that when the scan frequency is faster than the recombination and ionization rates, the charge balance remains stable, resulting in minimal oscillations in the ion population. Conversely, when it is lower than those rates, oscillations in the ion population become large.

In the present experiment, a slow scan frequency of 50 eV s^{-1} was employed due to technical limitations of the drift-tube high-voltage power supply. This means that when the electron beam passes through the strongest helium-like KLL resonance, which has a width of $\sim$7 eV, it spends about 140 ms on it. The strongest peak DR cross section is $\sim$5 × 10^{-20} cm^2. During this 140 ms period, the helium-like ion population will approximately decay according to exp($-n_e\,\sigma_e\,v_e\,dt$), where

Table 2
FAC-calculated DR Data for the Fe XXV Ion

n Shell[a]	$\|d\rangle$ Index[b]	$\|d\rangle$ Configuration[c]	$\|f\rangle$ Index[d]	$\|f\rangle$ Configuration[e]	Branching Ratio[f]	E_{beam} (eV)[g]	E_{photon} (eV)[h]	S_{DR} Strengths (cm^2 eV)[i]
2	271	$1s+1(1)1.2p-2(0)1$	98	$1s+2(0)0.2p-1(1)1$	9.8998E-01	4.6253E+03	6.6201E+03	6.9947E-23
2	271	$1s+1(1)1.2p-2(0)1$	99	$1s+2(0)0.2p+1(3)3$	6.4186E-03	4.6253E+03	6.6043E+03	4.5350E-25
2	270	$1s+1(1)1.2s+1(1)2.2p+1(3)3$	97	$1s+2(0)0.2s+1(1)1$	9.9999E-01	4.6181E+03	6.6625E+03	4.7348E-24
2	273	$1s+1(1)1.2p-1(1)0.2p+1(3)3$	98	$1s+2(0)0.2p-1(1)1$	2.9514E-03	4.6335E+03	6.6284E+03	2.7332E-24
2	273	$1s+1(1)1.2p-1(1)0.2p+1(3)3$	99	$1s+2(0)0.2p+1(3)3$	9.5362E-01	4.6335E+03	6.6125E+03	8.8311E-22
2	277	$1s+1(1)1.2p-1(1)2.2p+1(3)1$	98	$1s+2(0)0.2p-1(1)1$	7.6737E-01	4.6608E+03	6.6557E+03	1.2175E-21
2	277	$1s+1(1)1.2p-1(1)2.2p+1(3)1$	99	$1s+2(0)0.2p+1(3)3$	2.3053E-01	4.6608E+03	6.6399E+03	3.6575E-22
2	265	$1s+1(1)1.2s+2(0)1$	98	$1s+2(0)0.2p-1(1)1$	5.0987E-02	4.5556E+03	6.5505E+03	8.8268E-21
2	265	$1s+1(1)1.2s+2(0)1$	99	$1s+2(0)0.2p+1(3)3$	5.2411E-02	4.5556E+03	6.5347E+03	9.0733E-21
2	278	$1s+1(1)1.2p+2(4)5$	99	$1s+2(0)0.2p+1(3)3$	5.9891E-01	4.6653E+03	6.6443E+03	2.7967E-19
2	267	$1s+1(1)1.2s+1(1)2.2p-1(1)3$	97	$1s+2(0)0.2s+1(1)1$	9.8286E-01	4.5709E+03	6.6152E+03	5.7210E-22
2	274	$1s+1(1)1.2s+1(1)0.2p+1(3)3$	97	$1s+2(0)0.2s+1(1)1$	7.1247E-03	4.6358E+03	6.6801E+03	1.7592E-21

Notes. Four machine-readable tables corresponding to the He-like, Li-like, Be-like, and the B-like iron DR data are in the .tar.gz package.

[a] Principal quantum number of the shell in which the free electron is recombining during the dielectronic capture process.

[b] Index for the intermediate doubly excited states $|d\rangle$.

[c] Relativistic shell configuration of the $|d\rangle$states. Here, `2p+2(2)` represents two electrons in the $2p_{3/2}$ subshell with a total angular momentum $J = 1$, while `2p-2(2)` represents two electrons in the $2p_{1/2}$ subshell with $J = 1$. The number in parentheses indicates 2 times the total angular momentum of the coupled shell. Following the parentheses, a number representing the $2J$ value when all preceding shells are coupled is included. Therefore, `2p+2(2)2.2p-2(2)0` represents a state described as $[(2p_{3/2})^2_{(J=1)}(2p_{1/2})^2_{(J=1)}]_{J=0}$.

[d] Index for the final excited states $|f\rangle$. For each $|d\rangle$ state, there are several $|f\rangle$ states.

[e] Relativistic shell configuration of the $|f\rangle$ states.

[f] DR branching ratio.

[g] DR resonance energy in electron volts. This is also the electron-beam energy required to resonantly excite the $|d\rangle$ state.

[h] DR satellite photon energy in electron volts.

[i] DR resonance strength in cm^2 eV.

(This table is available in its entirety in machine-readable form in the online article.)
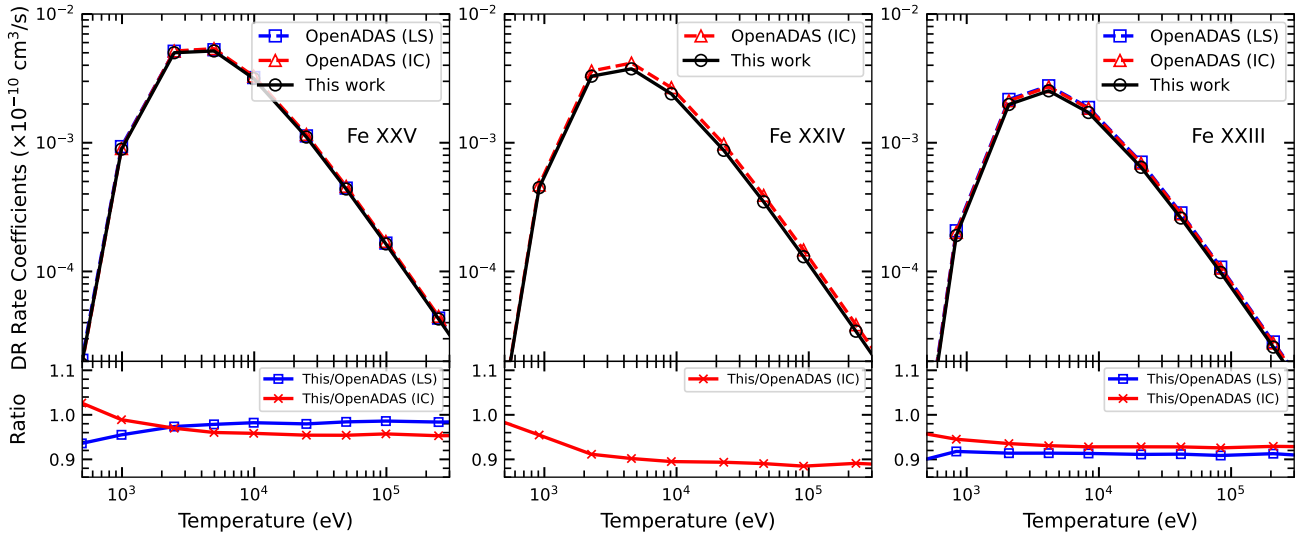
Figure 2. K-shell DR rate coefficients of Fe XXV–XXIII ions as a function of plasma electron temperature. The top panels show the comparison between the present DR rates and those available in the OPEN-ADAS database in their LS and IC coupling formats. The bottom panels display the ratio between the present and OPEN-ADAS rate coefficients.

n_e is the electron-beam density, σ_e is the cross section, v_e is the electron-beam velocity, and dt is the DR peak scan time. Assuming an effective electron density—i.e., considering the ion–electron beam fractional overlap factor—of approximately 10^{10} cm^{-3}, the helium-like population decreases by a factor of $\exp(-0.28)$, after scanning through the strongest DR resonance. Subsequently, the helium-like population recovers by electron-impact ionization at a slower rate. This complicates the comparison between experimental and theoretical resonance strengths as a function of the beam energy. To avoid this, we must determine the charge-state distribution in the present experiment.

Following the approach outlined by B. M. Penetrante et al. (1991a), we simulate the charge-state distribution by numerically solving 27 coupled differential equations, each of them describing the abundance of each charge state, with their ionization and recombination cross sections calculated by FAC. The simulation takes into account experimental parameters such as electron-beam energy and current, neutral gas density, and applied axial trap potential. We tested such simulations against experiments in our previous works (F. Grilo et al. 2021; W. Biela-Nowaczyk et al. 2023; F. Grilo et al. 2024). The simulated charge-state distribution during the upward scan is shown in Figure 3. As expected, it shows an overall increase of the helium-like abundance with growing electron beam energy and an instantaneous drop on the DR resonance with a corresponding jump of the lithium-like population. Similar patterns are observed for the other charge states studied in the present experiment.

The charge-state distribution does not change substantially in regions where no DR resonances are present, such as below the KLL, between the KLL and KLM resonances, and between KLM and KLN (see Figure 1). We first correct the intensities in the 2D plot for the cyclically varying electron-beam current density. Then, we extract projections of the spectrum along the RR ($n = 2$) band in these regions for cross-section calibration. Specifically, we first take 10 eV slices of data between KLL and KLM in the electron-beam energy range of 5480–5720 eV and project the summed spectrum onto the X-ray axis, as demonstrated in Figure 4(a). The observed RR intensity
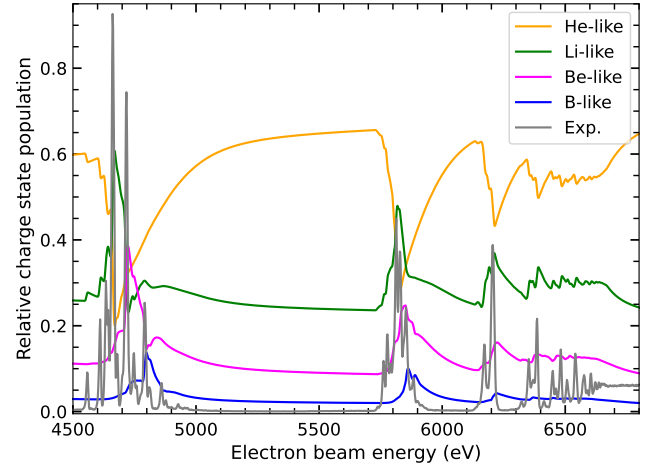

Figure 3. Predicted charge-state distribution of Fe ions trapped under the present experimental conditions. Summed DR satellite intensities within the Kα cut are superimposed to highlight the depletion of certain charge states caused by strong DR resonances at different resonance energies.

depends on both the RR cross sections at 90° with respect to the electron-beam propagation axis and the ion abundances in the EBIT. By calculating the angle-dependent RR cross sections, we can estimate the fractional charge-state distribution in the trap from this data, as shown in previous works (D. A. Knapp et al. 1989; P. Beiersdorfer et al. 1992a; A. J. Smith et al. 2000; H. Chen et al. 2005; Z. Harman et al. 2019; C. Shah et al. 2021).

The RR X-ray energies are the sum of the electron-beam energy and the binding energy of the ion state into which the electron recombines. For each slice of the electron-beam energy, we first calculate the RR X-ray energies and 90° RR cross sections using FAC. These calculations include the fine-structure component of each ion. The effective electron-beam energy differs from nominal because of the negative space charge of the electron beam compensated by the positive space charge of the ion cloud (F. Currell & G. Fussmann 2005). We therefore calibrated the electron beam energy using theoretical DR resonance energies. Using our calculated RR cross
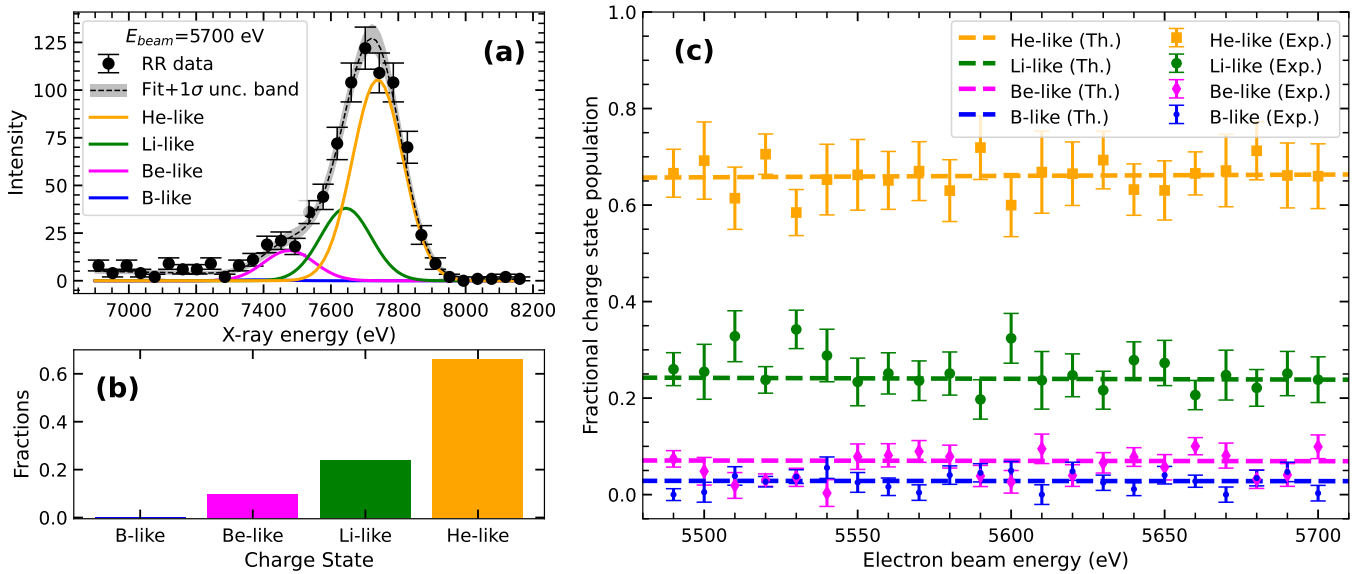
Figure 4. (a) Example fit to the radiative recombination (RR) into $n = 2$ data obtained from a 10 eV broad region of interest around an electron-beam energy of 5700 eV. (b) Fractional populations of charge states derived from this fit. (c) Derived fractional charge-state populations as a function of electron-beam energy based on the examples in (a) and (b). The extracted ion populations are compared with the theoretical charge balance simulation shown in Figure 3.

sections, we generate synthetic RR spectra for each ion by convolving the FAC-RR data on the photon-energy axis with a Gaussian function with 120 eV FWHM to account for the resolution of the SDD. The centroids and amplitudes of the synthetic spectrum for each charge state are then used as initial parameters for fitting the experimental RR data. In the fit, we fix the relative difference between peak centroids and share the widths of each peak while allowing the amplitudes to be free parameters. This allows us to obtain the relative charge balance of the trapped ions by taking the ratios of the fitted RR intensities and cross sections for each charge state. The resulting fit and the derived fractional charge-state distribution are shown for one energy slice in Figures 4(a) and (b). We repeat this procedure for all RR data slices to extract the charge-state distribution as a function of electron-beam energy. The results are in good agreement with our charge balance simulations, as shown in Figure 4(c), which further strengthens our confidence in these simulations.

Given that RR cross sections can be predicted within 3%–5% (D. A. Knapp et al. 1989; H. Chen et al. 2005), and the charge-state distribution is experimentally known, we can now derive a normalization factor for each charge state of Fe and infer DR cross sections, as demonstrated in Z. Harman et al. (2019) and C. Shah et al. (2021). However, predictions suggest that even with high electron-beam energy resolution of ∼7 eV, blending between resonances of different charge states persist. Thus, normalizing each charge state individually is challenging. Instead, we use the total RR counts divided by the product of fractional abundances and RR cross sections, i.e., an effective normalization factor defined as $I_{\mathrm{RR}}^{\mathrm{total}}/(\sum_{cs} n_{cs} \times \sigma_{cs}^{\mathrm{RR}})$, where (cs) indicates the charge state. Each RR slice in the KLL-KLM region gives the effective normalization factor. All factors are consistent within their statistical error bars. Thus, we took the weighted average of the normalization factor for the KLL-KLM range, which was found to be $(3.47 \pm 0.28) \times 10^{22}$ counts cm^{-2}.

The RR fit procedure is sensitive to uncertainties in the overall energy scale of the RR peaks, which are affected both by the energy scale calibration of the SDD as well as by the effective space charge of the electron beam. Both of these can

be modeled as a shift in the global energy scale of the RR complex, retaining the relative peak energies predicted by theory. We conservatively take the uncertainty on this energy scale as 10 eV and derive a systematic uncertainty of ∼4.5% on the normalization factor by shifting the energy scale and refitting the peaks. Furthermore, we considered a 5% uncertainty in the theoretical RR cross sections used for the normalization procedure. We add statistical and systematic uncertainties in quadrature and derive the effective normalization factor to be $(3.47 \pm 0.37) \times 10^{22}$ counts cm^{-2}. This value is then used to normalize measured DR intensities as a function of electron-beam energy, shown in Figure 5.

In addition to the RR $n = 2$ band between KLL and KLM, we apply the abovementioned procedure for the RR band below KLL in the electron-beam energy range of 4300–4500 eV, obtaining a normalization factor of $(3.48 \pm 0.34) \times 10^{22}$ counts cm^{-2}. The normalization factor for the RR band between KLM and KLN in the beam energy range of 5900–6100 eV is $(3.6 \pm 0.40) \times 10^{22}$ counts cm^{-2}. All normalization factors from different electron-beam energy regions, ranging from 4300 to 6100 eV, are consistent within their error bars, suggesting that the measurements are not significantly affected by variations in effective electron density and beam–ion overlap across the beam energy scan range and due to different charge states.

Finally, we compared our measured DR cross sections with FAC predictions weighted by the simulated charge-state distribution as a function of electron-beam energy (see Figure 5). We observe overall good agreement for the set of DR satellites contributing to the collisionally excited Kα, Kβ, Kγ, and K$n \geqslant 5$ X-ray lines. However, some discrepancies remain, such as the high-n satellites near the excitation threshold for Fe K-shell lines, which are slightly underestimated by the FAC calculations. This may be partly due to the exclusion of resonances with $n' > 15$ in our calculations. In addition, there are some differences in specific resonances: the KLN (Kγ) resonances at ∼6170 and ∼6190 eV, where the FAC predictions slightly exceed the measurements, and the KLM (Kα) resonance at
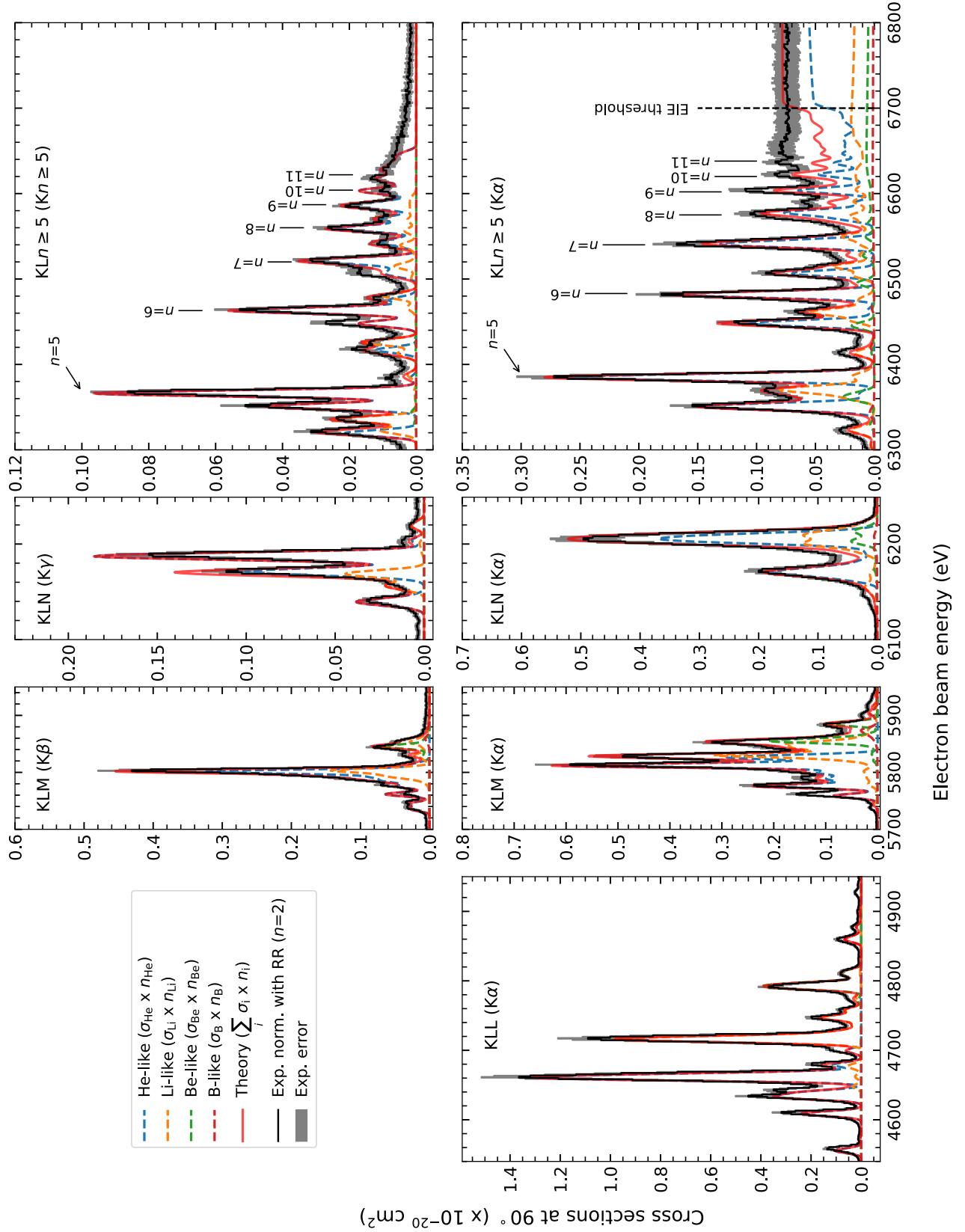
Figure 5. Total DR cross sections (black curve) measured at an angle of 90° with respect to the electron beam propagation axis and normalized to RR ($n = 2$) vs. electron-beam energy, with the total uncertainty shown as the gray band. Distorted wave predictions obtained with FAC for present charge-state distribution (see Figure 3) are shown as the red curve. Different charge-state components are also shown as dashed lines. Top three panels: projection of the KLn DR satellites from the RR ($n = 2$) slice in Figure 1. Bottom four panels: projection of the Kα slice from Figure 1.
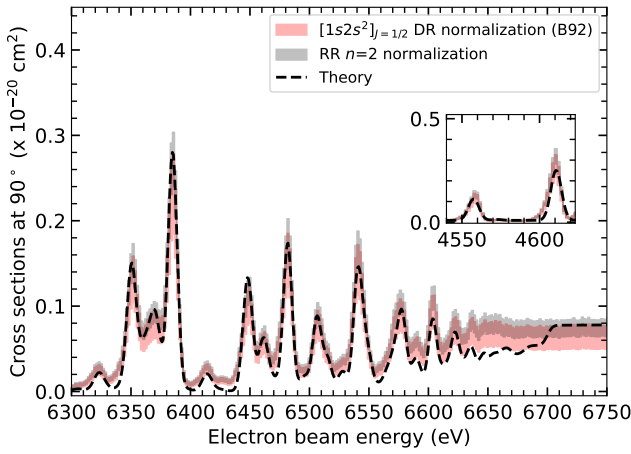
Figure 6. Comparison of present measurements normalized using one of the KLL resonances with the doubly excited state configuration, $[1s\,2s^2]_{J=1/2}$, as reported by P. Beiersdorfer et al. (1992a, B92 in the figure), with normalization using RR into $n = 2$ as observed here. The inset shows the region of normalization line, $[1s\,2s^2]_{J=1/2}$, at ~4554 eV (left peak). The dashed curve represents FAC predictions.

~5760 eV, where the FAC underestimates the cross sections. The reasons for these discrepancies are not yet clear. For beam energies above the excitation threshold ($\geqslant 6700$ eV), the measured electron impact cross sections for the Fe Kα line show good agreement with the FAC predictions. We also observe pileup counts above the Fe Kα satellites due to the high intensities of Fe L-shell photons near the 1 keV X-ray energy (see above KLL resonances in Figure 1). This may contribute to the count enhancement in the Kβ resonances as well as in the RR $n = 2$ band. However, we find that this contribution is less than 0.5% of the total counts, which means that it does not significantly affect our cross-section measurements.

We further validate our results by comparing them to the KLL DR satellite cross sections of Fe XXV measured by P. Beiersdorfer et al. (1992a) using the Lawrence Livermore National Laboratory EBIT (LLNL-EBIT) with an estimated uncertainty of 20%, mostly resulting from the response function and polarization sensitivity of the crystal spectrometer used there. For the comparison, we take the measured cross sections of the X-ray lines o and p underlying the first KLL DR resonance at an electron-beam energy of ~4554 eV. This DR resonance is interesting because its doubly excited state, $[1s\,2s^2]J = 1/2$, decays by two-electron-one-photon electric-dipole transitions with final states $[1s^2\,2p_{1/2,3/2}]_{J=1/2,3/2}$ for the o and p lines (X. Zhang et al. 2004), respectively.

Although this resonance is weak, it is well separated from the rest, and its doubly excited state with $J = 1/2$ leads to unpolarized, isotropic X-ray emission (C. Shah et al. 2018) and only causes a small depletion of the helium-like ion abundance. We take the sum of the o and p cross sections, corrected for the spectrometer response factor $G(s/w)$ as given in P. Beiersdorfer et al. (1992a), and obtain a normalization factor of $(4.08 \pm 0.82) \times 10^{22}$ counts cm^{-2}, with an uncertainty of approximately 20% mostly arising from that of the LLNL-EBIT measurements (P. Beiersdorfer et al. 1992a). This value is also in good agreement with the value inferred above from the RR $n = 2$ KLL-KLM energy band. The cross sections obtained

from two independent normalization methods are compared in Figure 6 and are consistent within their uncertainty limits and in agreement with the distorted-wave predictions for DR and EIE. This further confirms the uncertainty estimates of our resulting cross sections and comprehensively benchmarks FAC calculations involving RR, DR, and EIE processes.

4.2. L-shell Cross Sections: Cascades Following KLn $\geqslant$ 3 DR Satellites

Energetically below the primary K-shell DR satellite lines, we detected low-energy radiative cascades from resonances (e.g. $n = 3 \rightarrow 2$) where the spectator electron occupies the $n \geqslant 3$ shell. In the case of lithium-like KLN resonances, K-series decays such as $n = 4 \rightarrow 1$ and $n = 2 \rightarrow 1$ appear as a diagonal series of bright spots (see Figure 1) from high-n DR satellites alongside transitions such as $n = 4 \rightarrow 2$, $n = 4 \rightarrow 3$, and $n = 3 \rightarrow 2$ at energies below ~2 keV, as shown in Figure 7. As an example, the KLN resonances at ~1.5 keV and ~1.1 keV correspond to $n = 4 \rightarrow 2$ and $n = 3 \rightarrow 2$ decay paths, respectively. To obtain the cross sections for these low-energy cascades, we used our RR ($n = 2$) normalization factor. We first corrected the observed intensity for the 1 μm thick carbon foil in front of the X-ray detector using known transmission coefficients from B. L. Henke et al. (1993). This is more important for the low-energy L-shell X-rays than for those above 6 keV from K-shell vacancies. In our previous study (C. Shah et al. 2019), we validated the filter transmission below 2 keV using K-shell EIE lines and RR lines of O VIII and Ne X ions and found those coefficients agreeing within ~3%. We take into account this uncertainty in our normalization factor.

The continuous X-ray background seen around 1 keV is primarily due to $n = 3-2$ and $n = 4-2$ direct EIE of Fe XXIV–XX ions. These EIE components are typically linear at high electron-beam energies. Here, however, they modulate due to the changes in charge-state distribution as strong K-shell DR resonances are seen (see Figure 3). For instance, while scanning the KLN DR resonance of helium-like ion, the abundance of lithium-like ion increases, and accordingly the $n = 4 \rightarrow 2$ and $n = 3 \rightarrow 2$ emissions following the direct EIE of lithium-like ions. Outside the resonance, they are gradually ionized back to a helium-like charge state, and the lithium-like EIE emissions diminish, as apparent at beam energies above the resonances in Figure 7.

To model the L-shell spectrum, in addition to the DR cascades discussed in Section 3, we also computed with FAC direct EIE cross sections at 90° for $n = 3-2$ and $n = 4-2$ transitions in Fe XXIV–XX ions as a function of electron-beam energy. We compared our EIE predictions with previous experimental and theoretical results of M. F. Gu et al. (2001) and H. Chen et al. (2005) and found good agreement. The summed EIE and DR cross sections in the 1–2 keV range of X-ray energy, weighted by the charge-state distribution of each ion, are shown in Figure 7. These low-energy satellite cascades from K-shell DR satellites are critical for the complete spectral plasma modeling, as they blend with L-shell EIE lines for Fe XXV–XX ions, affecting the Fe L-shell spectrum.
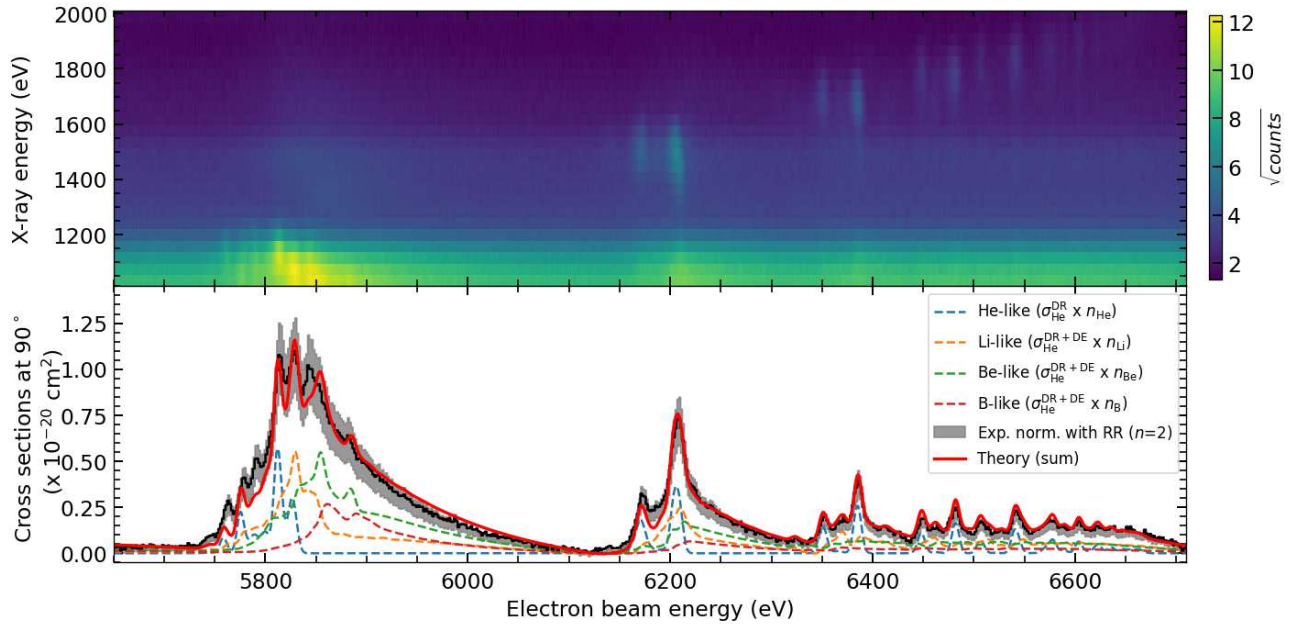
Figure 7. Top panel: 2D X-ray intensity histogram as a function of electron beam and X-ray energies. Bottom panel: summed X-ray intensity projected onto the electron-beam energy axis, normalized to the theoretical RR ($n = 2$) cross sections and corrected for the transmission of the filter on the X-ray detector. The different line emission components for each charge state, as predicted by the FAC, are also shown.

5. Summary and Conclusions

We present the most comprehensive measurements to date of K-shell DR resonances for Fe XXV–XXI ions, resolving KLn satellites up to $n' = 11$ with excellent electron–ion collision energy resolution and high counting statistics. This allowed us to determine cross sections for all observed DR satellites, normalized to those of RR into $n = 2$, with total uncertainties in cross sections well below 15%. We also compared these results with those from an *independent* normalization based on previous LLNL-EBIT measurements (P. Beiersdorfer et al. 1992a). We use the experimental cross sections to benchmark relativistic distorted-wave calculations performed using FAC (M. F. Gu 2008) and found overall an excellent agreement. Our investigation of low-energy lines below 2 keV due to cascades from $n \geqslant 3$ K-shell DR resonances and direct EIE process also found good agreement with the total L-shell cross sections predicted with FAC. This work thus comprehensively benchmarks K-shell and L-shell FAC calculations for astrophysically abundant Fe ions and underscores the suitability of this code for efficiently generating the large atomic data sets required for accurate modeling of astrophysical and fusion plasmas.

Our experimental and theoretical data can immediately be used to interpret existing spectra observed by Hitomi, Chandra, XMM-Newton, and Suzaku and will improve the analysis of high-resolution X-ray spectra currently from the X-ray microcalorimeter Resolve on board the XRISM observatory (XRISM Collaboration et al. 2024a, 2024b) and in the future from the planned Athena (F. Pajot et al. 2018) mission. With our results, a rigorous check of DR data used in the leading spectral modeling codes SPEX (J. S. Kaastra et al. 1996), CHIANTI (G. Del Zanna et al. 2015), and AtomDB (A. R. Foster et al. 2012) could perhaps explain the discrepancies those codes show in comparison with Hitomi observations (Hitomi Collaboration et al. 2018). In the future, experiments with miniature EBITs (P. Micke et al. 2018) capable of achieving twice as high electron-beam energy resolution than the work presented here in combination with a high-resolution, wide-band X-ray microcalorimeter (F. S. Porter et al. 2008, 2009; S. J. Smith et al. 2019; P. Szypryt et al. 2019; L. Gottardi & S. Smith 2024) capable of covering both K- and L-shell bands with an exceptional 2–5 eV resolution will further deepen our understanding of the DR process as dominant line-formation mechanism in plasmas and test atomic theory and plasma models more stringently than possible now. This is a crucial task toward fully exploiting the unique capabilities of present and upcoming X-ray observatories for understanding the role of high-energy X-ray sources in the evolution of galaxies, their clusters, and the intergalactic medium, where Fe emissions reveal the hottest components of the plasmas pervading them.

ORCID iDs

Chintan Shah ⓘ https://orcid.org/0000-0002-6484-3803
Pedro Amaro ⓘ https://orcid.org/0000-0002-5257-6728
Filipe Grilo ⓘ https://orcid.org/0000-0001-5777-1891
Ming Feng Gu ⓘ https://orcid.org/0000-0001-9136-8449
Liyi Gu ⓘ https://orcid.org/0000-0001-9911-7038
José Paulo Santos ⓘ https://orcid.org/0000-0002-5890-0971
F. Scott Porter ⓘ https://orcid.org/0000-0002-6374-1119
Thomas Pfeifer ⓘ https://orcid.org/0000-0002-5312-3747
Maurice A. Leutenegger ⓘ https://orcid.org/0000-0002-3331-7595
José R. Crespo López-Urrutia ⓘ https://orcid.org/0000-0002-2937-8037

References

Ali, S., Mahmood, S., Orban, I., et al. 2011, JPhB, 44, 225203
Amaro, P., Shah, C., Steinbrügge, R., et al. 2017, PhRvA, 95, 022712
Asplund, M., Amarsi, A. M., & Grevesse, N. 2021, A&A, 653, A141
Azarov, V. I., Kramida, A., & Ralchenko, Y. 2023, ADNDT, 149, 101548
Badnell, N. R. 1986, JPhB, 19, 3827
Bautista, M. A., & Badnell, N. R. 2007, A&A, 466, 755
Beiersdorfer, P. 2003, ARA&A, 41, 343
Beiersdorfer, P., Phillips, T., Jacobs, V. L., et al. 1993, ApJ, 409, 846
Beiersdorfer, P., Phillips, T. W., Wong, K. L., Marrs, R. E., & Vogel, D. A. 1992a, PhRvA, 46, 3812
Beiersdorfer, P., Schneider, M. B., Bitter, M., & von Goeler, S. 1992b, RScI, 63, 5029
Beiersdorfer, P., Osterheld, A. L., Chen, M. H., et al. 1990, PhRvL, 65, 1995
Beiersdorfer, P., Vogel, D. A., Reed, K. J., et al. 1996, PhRvA, 53, 3974
Beilmann, C., Mokler, P. H., Bernitt, S., et al. 2011, PhRvL, 107, 143201
Beilmann, C., Postavaru, O., Arntzen, L. H., et al. 2009, PhRvA, 80, 050702
Bely-Dubau, F., Gabriel, A. H., & Volonte, S. 1979, MNRAS, 186, 405
Bianchi, S., Matt, G., Nicastro, F., Porquet, D., & Dubau, J. 2005, MNRAS, 357, 599
Biela-Nowaczyk, W., Amaro, P., Grilo, F., et al. 2023, Atoms, 11
Burgess, A. 1964, ApJ, 139, 776
Bykov, A. M., Paerels, F. B. S., & Petrosian, V. 2008, SSRv, 134, 141
Chen, H., Beiersdorfer, P., Scofield, J. H., et al. 2005, ApJ, 618, 1086
Chen, M. H. 1986, ADNDT, 34, 301
Colgan, J., Pindzola, M. S., & Badnell, N. R. 2004, A&A, 417, 1183
Colgan, J., Pindzola, M. S., Whiteford, A. D., & Badnell, N. R. 2003, A&A, 412, 597
Currell, F., & Fussmann, G. 2005, ITPS, 33, 1763
Decaux, V., Beiersdorfer, P., Kahn, S. M., & Jacobs, V. L. 1997, ApJ, 482, 1076
Decaux, V., Beiersdorfer, P., Osterheld, A., Chen, M., & Kahn, S. M. 1995, ApJ, 443, 464
Del Zanna, G., Dere, K. P., Young, P. R., Landi, E., & Mason, H. E. 2015, A&A, 582, A56
Dubau, J., & Volonte, S. 1980, RPPh, 43, 199
Ebisawa, K., Ueda, Y., Inoue, H., Tanaka, Y., & White, N. E. 1996, ApJ, 467, 419
Epp, S. W., López-Urrutia, J. R. C., Brenner, G., et al. 2007, PhRvL, 98, 183001
Epp, S. W., Crespo López-Urrutia, J. R., Simon, M. C., et al. 2010, JPhB, 43, 194008
Fabian, A. C. 2023, in High-Resolution X-Ray Spectroscopy: Instrumentation, Data Analysis, and Science, ed. C. Bambi & J. Jiang (Berlin: Springer), 3
Foster, A. R., Ji, L., Smith, R. K., & Brickhouse, N. S. 2012, ApJ, 756, 128
Fuchs, T., Biedermann, C., Radtke, R., Behar, E., & Doron, R. 1998, PhRvA, 58, 4518
Gabriel, A. H., & Jordan, C. 1969, MNRAS, 145, 241
González Martínez, A. J., López-Urrutia, J. R. C., Braun, J., et al. 2005, PhRvL, 94, 203201
Gottardi, L., & Smith, S. 2024, in Handbook of X-Ray and Gamma-Ray Astrophysics, ed. C. Bambi & A. Santangelo (Berlin: Springer), 709
Grilo, F., Shah, C., Marques, J., et al. 2024, PhRvA, 110, 042827
Grilo, F., Shah, C., Kühn, S., et al. 2021, ApJ, 913, 140
Gu, L., Shah, C., Mao, J., et al. 2020, A&A, 641, A93
Gu, M. F. 2003, ApJ, 590, 1131

Gu, M. F. 2008, CaJPh, 86, 675
Gu, M. F., Kahn, S. M., Savin, D. W., et al. 2001, ApJ, 563, 462
Gu, M. F., Kahn, S. M., Savin, D. W., et al. 1999, ApJ, 518, 1002
Harman, Z., Shah, C., González Martínez, A. J., et al. 2019, PhRvA, 99, 012506
Harra-Murnion, L. K., Phillips, K. J. H., Lemen, J. R., et al. 1996, A&A, 308, 670
Henderson, J. R., Beiersdorfer, P., et al. 1990, PhRvL, 65, 705
Henke, B. L., Gullikson, E. M., & Davis, J. C. 1993, ADNDT, 54, 181
Hitomi Collaboration, Aharonian, F., Akamatsu, H., et al. 2016, Natur, 535, 117
Hitomi Collaboration, Aharonian, F., Akamatsu, H., et al. 2018, PASJ, 70, 12
Hu, Z., Li, Y., & Nakamura, N. 2013, PhRvA, 87, 052706
Kaastra, J. S., Ferrigno, C., Tamura, T., et al. 2001, A&A, 365, L99
Kaastra, J. S., Mewe, R., & Nieuwenhuijzen, H. 1996, in UV and X-Ray Spectroscopy of Astrophysical and Laboratory Plasmas, ed. K. Yamashita & T. Watanabe (Cambridge: Cambridge Univ. Press), 411
Kato, T., Fujiwara, T., & Hanaoka, Y. 1998, ApJ, 492, 822
Knapp, D. A., Marrs, R. E., Levine, M. A., et al. 1989, PhRvL, 62, 2104
Knapp, D. A., Marrs, R. E., Schneider, M. B., et al. 1993, PhRvA, 47, 2039
Lukić, D. V., Schnell, M., Savin, D. W., et al. 2007, ApJ, 664, 1244
Massey, H. S. W., & Bates, D. R. 1942, RPPh, 9, 62
Micke, P., Kühn, S., Buchauer, L., et al. 2018, RScI, 89, 063109
Miller, J. M., Raymond, J., Reynolds, C. S., et al. 2008, ApJ, 680, 1359
Nahar, S. N., Pradhan, A. K., & Zhang, H. L. 2001, ApJS, 133, 255
Nakamura, N., Kavanagh, A. P., Watanabe, H., et al. 2008, PhRvL, 100, 073203
Nandra, K. 2006, MNRAS, 368, L62
Nicastro, F., Kaastra, J., Krongold, Y., et al. 2018, Natur, 558, 406
Nicastro, F., Mathur, S., & Elvis, M. 2008, Sci, 319, 55
Nilsen, J. 1988, ADNDT, 38, 339
Oppenheimer, J. R. 1927, PNAS, 13, 800
Orban, I., Loch, S. D., Böhm, S., & Schuch, R. 2010, ApJ, 721, 1603
O'Rourke, B. E., Kuramoto, H., Li, Y. M., et al. 2004, JPhB, 37, 2343
Pajot, F., Barret, D., Lam-Trong, T., et al. 2018, JLTP, 193, 901
Penetrante, B. M., Bardsley, J. N., DeWitt, D., Clark, M., & Schneider, D. 1991a, PhRvA, 43, 4861
Penetrante, B. M., Bardsley, J. N., Levine, M. A., Knapp, D. A., & Marrs, R. E. 1991b, PhRvA, 43, 4873
Peterson, J. R., Paerels, F. B. S., Kaastra, J. S., et al. 2001, A&A, 365, L104
Porquet, D., Dubau, J., & Grosso, N. 2010, SSRv, 157, 103
Porter, F. S., Beiersdorfer, P., Brown, G. V., et al. 2008, JLTP, 151, 1061
Porter, F. S., Beiersdorfer, P., Brown, G. V., et al. 2009, JPhCS, 163, 012105
Radtke, R., Biedermann, C., Fuchs, T., Fußmann, G., & Beiersdorfer, P. 2000, PhRvE, 61, 1966
Reimers, D. 2002, SSRv, 100, 89
Rudolph, J. K., Bernitt, S., Epp, S. W., et al. 2013, PhRvL, 111, 103002
Sardar, S., Wang, S.-X., & Zhu, L.-F. 2018, ApJ, 869, 128
Savin, D. W., Behar, E., Kahn, S. M., et al. 2002a, ApJS, 138, 337
Savin, D. W., Kahn, S. M., Linkemann, J., et al. 2002b, ApJ, 576, 1098
Schnell, M., Gwinner, G., Badnell, N. R., et al. 2003, PhRvL, 91, 043001
Shah, C., Amaro, P., Steinbrügge, R., et al. 2016, PhRvE, 93, 061201
Shah, C., Amaro, P., Steinbrügge, R., et al. 2018, ApJS, 234, 27
Shah, C., Crespo López-Urrutia, J. R., Gu, M. F., et al. 2019, ApJ, 881, 100
Shah, C., Jörg, H., Bernitt, S., et al. 2015, PhRvA, 92, 042702
Shah, C., Hell, N., Hubbard, A., et al. 2021, ApJ, 914, 34
Smith, A. J., Beiersdorfer, P., Widmann, K., Chen, M. H., & Scofield, J. H. 2000, PhRvA, 62, 052717
Smith, S. J., Adams, J. S., Bandler, S. R., et al. 2019, Proc. SPIE, 5, 021008
Steinbrügge, R., Kühn, S., Nicastro, F., et al. 2022, ApJ, 941, 188
Sterling, A. C., Hudson, H. S., & Watanabe, T. 1997, ApJ, 479, L149
Szypryt, P., O'Neil, G. C., Takacs, E., et al. 2019, RScI, 90, 123107
Tamura, T., Bleeker, J. A. M., Kaastra, J. S., Ferrigno, C., & Molendi, S. 2001, A&A, 379, 107
Tashiro, M., Maejima, H., Toda, K., et al. 2018, Proc. SPIE, 10699, 1069922
Tiesinga, E., Mohr, P. J., Newell, D. B., & Taylor, B. N. 2021, RvMP, 93, 025010
Vainshtein, L. A., & Safronova, U. I. 1978, ADNDT, 21, 49
Watanabe, H., Currell, F. J., Kuramoto, H., et al. 2001, JPhB, 34, 5095
Widmann, K., Beiersdorfer, P., Decaux, V., et al. 1995, RScI, 66, 761
XRISM Collaboration, Audard, M., Awaki, H., et al. 2024a, ApJL, 977, L34
XRISM Collaboration, Audard, M., Awaki, H., et al. 2024b, ApJL, 973, L25
Yao, K., Geng, Z., Xiao, J., et al. 2010, PhRvA, 81, 022714
Yerokhin, V. A., & Surzhykov, A. 2012, PhRvA, 86, 042507
Yerokhin, V. A., & Surzhykov, A. 2018, JPCRD, 47, 023105
Zhang, X., López-Urrutia, J. R. C., Guo, P., et al. 2004, JPhB, 37, 2277